Solid-State Zinc Ion Hybrid Capacitor Using MWCNTs Cathode

*Antima Pandey, Shanu Mishra, Ashish Kumar Mishra**

School of Materials Science and Technology,

Indian Institute of Technology (Banaras Hindu University), Varanasi, India.

Email: akmishra.mst@iitbhu.ac.in

Abstract

In this study, multiwalled carbon nanotubes (MWCNTs) were synthesized using iron nanoparticles as catalyst, derived from green tea. We demonstrated a zinc ion hybrid capacitor cell utilizing MWCNTs as a cathode. The cell achieved a specific capacitance of 221 F g^{-1} at a current density of 1 A g^{-1}, showcasing superior rate capability with 93.7 F g^{-1} at 5 A g^{-1}. Additionally, it exhibited a high energy density of 78.9 W h kg^{-1} and a power density of 800 W kg^{-1} at 1 A g^{-1}. After 8000 charge-discharge cycles, tested at 5 A g^{-1}, the cell retained 89% of its capacitance retention with nearly 100% coulombic efficiency.

Keywords: *Zinc ion hybrid capacitor; Polyvinyl alcohol; Zinc sulphate; Multiwalled carbon nanotube, Specific capacitance.*

1. Introduction

Electrochemical energy storage devices (EES) have garnered significant attention in achieving economic and low-carbon societies due to their high energy/power densities, ease of design, and environmental sustainability [1,2]. These devices encompass various types such as metal-ion batteries (e.g., Li, Na, K, Zn), supercapacitors, and hybrid capacitors [3,4]. Hybrid capacitors, which combine a battery-type electrode and a capacitor-type electrode, offer high energy and power densities along with extended cycle life [5]. Among hybrid capacitors, zinc-ion hybrid capacitors (ZIHCs) are particularly noteworthy [6]. They utilize a battery-type zinc metal anode and a capacitor-type carbon cathode to achieve their performance characteristics. Compared to Li/Na-ion hybrid capacitors, ZIHCs are advantageous due to their lower cost and enhanced safety profiles [7]. ZHCs typically consist of Zinc (Zn) metal anodes, which offer a high theoretical specific capacity of 823 m Ah g^{-1} and operate at a low redox potential (-0.76 V versus standard hydrogen electrode) [8]. The carbon cathode serves as the capacitor-type electrode. Aqueous or polymer-based solid electrolytes containing Zn^{2+} ions, facilitate efficient energy storage [9]. The combination of these components enables ZIHCs to store energy effectively, maintain a wide voltage window, and demonstrate robust performance in various applications. Since, Carbon cathodes are characterized by their high specific surface area, extensive porous structure, and excellent electrical conductivity, which facilitate rapid adsorption and desorption of zinc-containing ions [10]. These properties contribute significantly to achieve high power densities in ZIHCs. However, carbon cathode materials still confront challenges related to their reversible charge storage capacity [11]. This issue predominantly stems from factors such as the energy storage mechanism along with the physical and chemical properties of carbon materials [12]. These factors include mismatched pore sizes with zinc ions, low density, and underutilization of active sites. Therefore, the pivotal strategy to enhance the zinc ion storage capabilities of ZIHCs lies in the design and advancement of novel porous carbon cathode materials [13]. This approach aims to optimize the microstructure and surface properties of carbon materials, thereby maximizing their efficiency in storing and releasing zinc ions during electrochemical processes [14]. Various precursors have been utilized to manufacture high-specific surface area activated carbon as cathode materials for ZIHCs, including biomass such as sugarcane stems, glutinous rice, and bamboo shavings [15–17].

Polymers like polyaniline-co-polypyrrole-derived hollow carbon spheres and polyacrylonitrile-derived carbon have also been employed [18–23]. Solid electrolytes are typically non-flammable and less prone to leakage compared to liquid electrolytes, enhancing the safety of devices such as batteries, they can operate at higher voltages without decomposition or side reactions, which improves the stability and lifespan of the device. Solid electrolytes enable higher energy density designs due to their ability to pack more active materials in a given volume or weight compared to liquid electrolytes. They can function effectively over a wider range of temperatures compared to liquid electrolytes, making them suitable for diverse environmental conditions. Certain solid electrolytes exhibit resistance to dendrite formation, a common issue in batteries that can cause short circuits and reduce lifespan. They can contribute to environmentally friendly devices by reducing the use of flammable and toxic materials typically found in liquid electrolytes. Solid electrolytes are promising for advancing the performance, safety, and environmental impact of energy storage devices such as batteries and capacitors [24–29]. Additionally, some literature described polymer electrolyte-based ZIHCs utilizing carbon materials as a cathode. Wei *et al*. [30] used carbon fiber as a cathode and showed a specific capacity of 47.6 m A h g^{-1} at 0.2 A g^{-1}, maintaining 78% capacitance retention over 5000 cycles. Wang *et al*. [31] demonstrated ZIHCs using bio-carbon-derived porous material as the cathode, showing a good discharge capacitance of 170 F g^{-1} at 0.1 A g^{-1} with high energy density (52.7 W h kg^{-1} at 1725 W kg^{-1} power density). Chen *et al*. [32] synthesized co-polymer-derived hollow carbon spheres as cathode and demonstrated that the flexible solid-state ZIHC shows maximum capacity of 86.8 m A h g^{-1} and an energy density of 59.7 W h kg^{-1} with a power density of 447.8 W kg^{-1}.

There have been few studies on green approach for the synthesis of carbon nanotubes (CNTs). Tripathi *et al*. presented a novel approach and demonstration the growth of bulk carbon nanotubes (CNTs) using green catalysts. The CNTs were synthesized using catalysts derived from plant extracts, specifically garden grass (Cynodon dactylon), rose (Rosa), neem (Azadirachta indica), and walnut (Juglans regia) [33]. Chufa *et al*. highlighted recent advancements in carbon nanotube (CNT) synthesis, with particular emphasis on green synthesis methods [34]. In this study the authors used green tea to synthesize stable iron nanoparticles and employed iron nanoparticles as catalysts to prepare MWCNTs via CVD method through pyrolysis of acetylene. Here, we introduced a safe solid-state zinc ion hybrid supercapacitor (ZIHC) with MWCNTs as cathode, polyvinyl alcohol/zinc sulphate (PVA + $ZnSO_4$) membrane as electrolyte, and zinc sheet as anode. The ion adsorption and desorption kinetics of the cathode is improved due to the high surface area of the MWCNTs and their nanotube structure. The designed solid-state ZIHC shows good specific capacitance and energy density with a high-power density along with a high degree of capacitance retention.

2 Experimental

2.1 Materials

Ferrous sulfate heptahydrate ($FeSO_4 \cdot 7H_2O$) and nitric acid (HNO_3) were purchased from Loba Chemie Pvt. Ltd., India, while the lepton green tea leaves were obtained from a local commercial vendor. The chemical reagents were of analytical grade and were employed without additional purification.

2.2 Synthesis of Multiwalled Carbon Nano Tubes (MWCNTs)

Synthesis of iron nanoparticles using green tea (Lipton green tea) extract and MWCNTs are done as described in our earlier report [35]. Lipton Green Tea consists of Camellia Sinensis leaves that have undergone minimal oxidation during processing to preserve the natural polyphenols and antioxidants present in the leaves. Green tea helps to stabilize the iron nanoparticles which act as catalyst for the growth of CNTs. The stable iron nanoparticles provide greater yield of CNTs using C_2H_2 as precursor. The conventionally synthesized iron

nanoparticles get easily oxidized, which reduces their catalytic activity and hence decreases the yield of CNTs. Specifically, 2.5 g of ferrous sulphate was added to 40 mL of prepared green tea extract, and the mixture was continuously stirred for 24 hours. During this period, the green tea extract served as a reducing agent and reduces ferrous sulphate into zero-valent iron nanoparticles. The resulting solution was then centrifuged and subsequently dried. An advantageous aspect of green tea-synthesized iron nanoparticles lies in dual role of green tea extract acting as a dispersant and capping agent. This property prevents nanoparticle agglomeration and enhances their stability, thereby prolonging their reactivity.

The prepared iron nanoparticles as catalyst were placed in quartz boat and positioned in a chemical vapor deposition (CVD) setup. The quartz boat underwent heating to 700 °C at a rate of 5 °C/min under an inert Ar-H_2 atmosphere with flow rate of 100 sccm. Subsequently, acetylene, a carbon source gas, was introduced into the quartz tube at 700 °C with a flow rate of 100 sccm for 30 minutes to facilitate the growth of multi-walled carbon nanotubes (MWCNTs). After the growth period of 30 minutes, the furnace was cooled to room temperature. The as-synthesized nanotubes underwent further treatment by heating at 400 °C for 120 minutes in open air to remove any amorphous carbon impurities. This step was followed by an acid purification process: the carbonized sample was mixed with 40 mL of concentrated nitric acid and stirred on a magnetic stirrer at 80 rpm for 24 hours. The resulting product was washed with deionized water until neutral and collected via centrifugation. Finally, the nanotubes obtained were dried in a vacuum oven at 60 °C.

2.3 Characterization

The synthesized MWCNTs was analyzed using various characterization techniques. X-ray diffraction (XRD) pattern was obtained in the 2θ range of 10–65° using a Rigaku Miniflex-600 with Cu Kα radiation (λ = 0.154 nm), employing a step size of 0.02°. Surface morphology was examined using a scanning electron microscope (Nova Nano SEM 450) operating at 20 kV, while high-resolution transmission electron microscopy (TEM Tecnai G20 TWIN) was used for detailed structural analysis. The Raman spectrum of the MWCNTs sample was acquired using a STR-300 micro-Raman spectrometer, with a laser excitation wavelength of 532 nm and a step size of 1.2 cm^{-1} with 1200 grating. FTIR study was done using a ThermoFisher Nicolet summit spectrometer using KBr pellets with a 4 cm^{-1} resolution.

2.4 Preparation of electrodes for electrochemical measurements

A uniform slurry solution of MWCNTs electrocatalyst was prepared by ultrasonically dispersing 10 mg of MWCNTs in 80 µL isopropyl alcohol, supplemented with 5 µL of Nafion as a binder. Conducting carbon paper (procured from Sainergy Fuel Cell India Pvt. Ltd., Chennai, India) sized at 1 cm × 1 cm was coated with the prepared slurry using a brush coating technique. Subsequently, the electrodes were dried overnight in a vacuum oven at 120 °C to minimize the effects of the binder.

For electrochemical measurements, a three-electrode setup was employed with Ag/AgCl (saturated with KCl) and Pt wire serving as reference and counter electrodes, respectively. The working electrode consisted of MWCNTs coated conducting carbon paper with a mass loading of 2 mg. Electrochemical characterization involved cyclic voltammetry (CV) at different scan rates within a voltage range of 0.0 to 0.9 V. All measurements were conducted in a 2 M $ZnSO_4$ aqueous electrolyte using a Corr Test electrochemical workstation instrument. A solid-state zinc ion hybrid capacitor device was tested within a potential range of 0.2 to 1.8 V. Electrochemical impedance spectroscopy (EIS) studies of MWCNTs were performed across frequencies ranging from 0.01 to 10^5 Hz, using a voltage amplitude of 5 mV.

2.5 Preparation of solid electrolyte and solid zinc ion hybrid capacitor cell

To prepare the PVA-$ZnSO_4$ gel membrane, 2 g of PVA was dissolved in 20 mL of deionized water at 90°C with vigorous stirring until the solution turned

transparent. Once completely dissolved, 2M $ZnSO_4$ solution was prepared in 5 mL of deionized water was mixed into the PVA solution. The mixture was allowed to cool to room temperature, then poured into the patterned disc and subjected to freeze-drying at - 15°C for 12h to get final membrane.

ZIHC system was assembled using MWCNT-coated carbon paper as cathode and Zinc sheet as anode having dimensions of 2×2 cm^2. A PVA-$ZnSO_4$ solid membrane was placed between the two electrodes, which acts as a separator and electrolyte. The cathode was mounted on one side using a stainless-steel sheet as a current collector.

3 Results and discussion

3.1 Morphology, structural and spectroscopic studies

The scanning electron microscopy (SEM) analysis of purified MWCNTs, depicted in Fig. 1(a), reveals a uniform distribution of numerous curled and loosely entangled nanotubes. The image also verifies the purity of the MWCNTs by showing no presence of amorphous carbon or residual metal catalyst particles. The observed shorter lengths of the nanotubes are attributed to the rigorous acid treatment, which likely also contributed to the opening of hemispherical caps at the ends of the MWCNTs. Additionally, the structural morphology was investigated using transmission electron microscopy (TEM) as shown in Fig. 1(b). This examination confirmed the presence of MWCNTs with varied outer diameters ranging from 60 to 80 nm. The TEM image also revealed entangled and curled nanotubes, along with sidewall defects induced by the strong acid treatment. The crystallinity of purified MWCNTs was assessed through X-ray diffraction (XRD) analysis. The XRD pattern of MWCNTs closely resemble those of graphite due to their intrinsic nature [36]. The XRD pattern of MWCNTs (Fig. 1 c) exhibits characteristic peaks at 25.9° and 42.5°, corresponding to the (002) and (100) diffraction planes, respectively. The sharper peak around 25.9° is attributed to graphitic carbon. Compared to the standard graphite peak at $2\theta = 26.5°$, MWCNTs exhibit a slight shift towards a lower θ value, indicating an increased interlayer spacing of the sp^2 carbon layers [37]. The degree of crystallinity and defects in purified MWCNTs were analyzed using Raman spectroscopy. The Raman spectrum of MWCNTs exhibits two prominent bands: the D band (~1332 cm^{-1}) and the G band (~1602 cm^{-1}), as illustrated in Fig. 1 (d). The D band arises from the out-of-plane vibrations of sp^3-hybridized carbon atoms, indicating disordered graphitic planes and surface defects induced by the acid treatment during purification [38]. On the other hand, the G band corresponds to the in-plane stretching vibration of sp^2 carbon atoms. The intensity ratio (I_D/I_G) of the D and G bands in the Raman spectrum of MWCNTs was approximately 0.89. This indicates that the MWCNTs possess noticeable defects and functional groups resulting from the acid treatment, which likely contribute to reducing charge transfer resistance during the electrochemical processes [39]. The FTIR spectrum, shown in Figure 2(e) for MWCNTs, indicates the presence of various functional groups such as hydroxyl, carboxylic, and carbonyl groups. The FTIR spectrum reveals several distinctive peaks: a prominent O-H stretching vibration at approximately 3437 cm^{-1}, indicating the presence of hydroxyl groups (-OH) in the MWCNTs. Another significant peak appears around 2920 cm^{-1}, corresponding to C-H stretching vibrations, suggesting the existence of carbon-hydrogen (C-H) bonds. Additionally, there is a distinct peak at approximately 1730 cm^{-1}, attributed to the C=O bond stretching vibration, indicating the presence of carbonyl groups (C=O) in MWCNTs. The sharper and stronger C=C peak at around 1650 cm^{-1} in MWCNTs suggests a longer-range order of the sp^2 network. which provides better electrochemical behavior for the MWCNTs.

3.2 Electrochemical study

To investigate the electrocatalytic behavior of the prepared materials, electrochemical active surface area (ECSA) analysis was conducted using the cyclic voltammetry (CV) technique [40]. CV scans were performed at different scan rates (20, 40, 60, 80, and 100 mV s^{-1}) for MWCNTs (Fig. 2 a), in the non-faradaic region between -0.25 and 0.25 V.

To determine the double-layer capacitance (C_{dl}), half of the average difference between the anodic and cathodic charging currents at 0 V was linearly plotted against the scan rates, as shown in Fig.3 (b). The slope of this plot provides the C_{dl} value [35]. The electrochemical-specific surface area was calculated from the following equation (1).

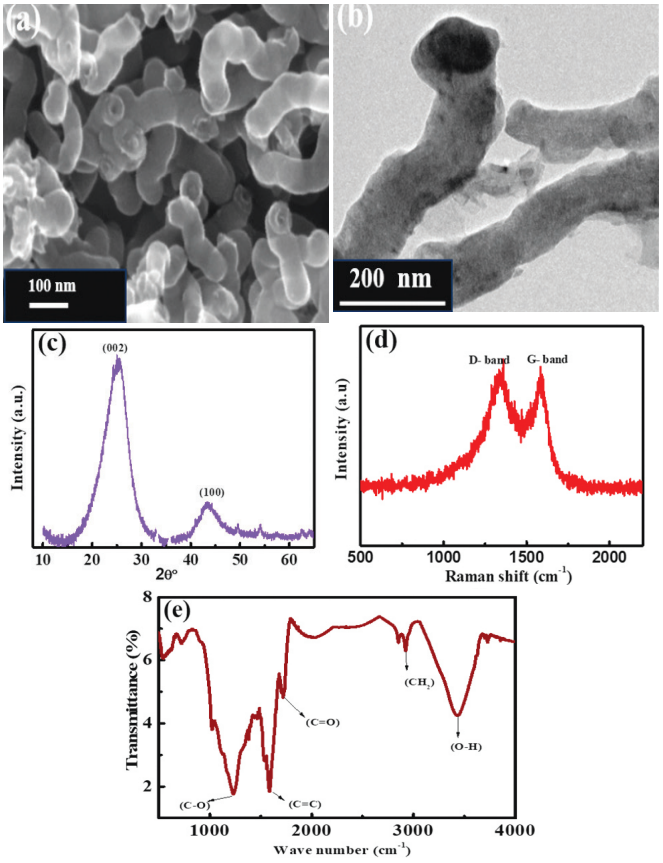


Fig.1 ***(a)*** *SEM image*, ***(b)*** *TEM image* ***(c)*** *XRD pattern*, ***(d)*** *RAMAN spectrum,* and *(e)FTIR spectrum of MWCNTs.*

$$ECSA = \frac{C_{dl}}{C_s} \quad (1)$$

Where C_{dl} represents the double-layer capacitance and C_S is the specific capacitance of the ideal flat surface of the catalyst. Various capacitance values for C_S within the range of 20-80 µF/cm² have been reported, with a commonly cited value being 40 µF/cm² [41]. The MWCNT material's C_{dl} value was investigated at 70.3 mF, and C_s was specified with a specific capacitance value of 40 µF. The estimated effective surface area (ECSA) of the MWCNT nanostructure is ~1757 cm². Given that the total mass of the MWCNT electrode is 2 mg, the available ECSA will be ~878 cm² mg^{-1}, which provides high charge storage in ZIHC.

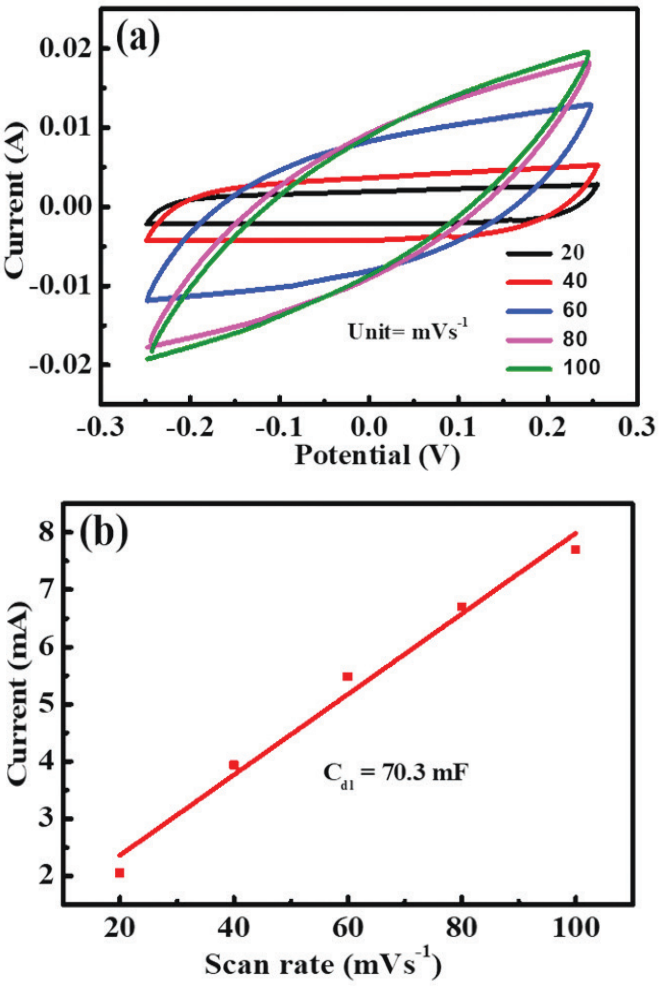


Fig.2 ***(a)*** *Electrochemical active surface Area (ECSA) test*, ***(b)*** *Half of the difference of anodic and cathodic currents vs voltage scan rate for MWCNTs.*

Cyclic voltammetry (CV), galvanostatic charge-discharge (GCD), and electrochemical impedance spectroscopy (EIS) measurements were conducted using a three-electrode system to explore the capacitive properties of MWCNT-coated carbon paper electrodes. These tests were performed within a potential range of 0 to 0.9 V using a 2 M $ZnSO_4$ aqueous electrolyte. Figure 3 (a) illustrates the schematic representation of the 3-cell measurement setup. The setup includes an Ag/AgCl reference electrode, a Pt wire as the counter electrode, and the working electrode composed of the MWCNTs coated on carbon paper. Fig 3 (b) illustrates the CV curves

obtained for the MWCNTs electrodes at various scan rates. The substantial area enclosed by the CV curves indicates the excellent capacitive behavior of the MWCNTs[42]. The specific capacitance of MWCNTs from CV study can be calculated using the following equation (2).

$$\text{Specific capacitance} = \frac{\int \text{Area inclosed in the CV curve}}{m \times \Delta V \times S} \quad (2)$$

where m is the mass loading of MWCNTs on the electrode, ΔV is the potential window of the CV measurement, and S is the voltage scan rate. This formula allows for determining the specific capacitance based on the experimental data obtained from CV measurements. The maximum specific capacitance of ~151 F g^{-1} was observed for MWCNTs at 5 mV s^{-1}. The quasi-rectangular behavior in the CV curves for MWCNTs indicates the formation of an electrical double layer at the electrode-electrolyte interface. The maximum specific capacitance of 62.7 F g^{-1} was obtained at a high scan rate of 100 mV s^{-1}, suggesting a high degree of sustainability of capacitive performance, as shown in Fig. 3 (c). The capacitive characteristic can also be assessed through constant current charge-discharge cyclic testing, offering a more quantitative perspective on the capacitive performance of electrode material. Equation (3) was employed to calculate the specific capacitance (Cs) using the charge-discharge method.

$$\text{Specific capacitance} = \frac{I}{m} \text{X} \frac{\Delta t}{\Delta V} \quad (3)$$

where Δt represents the discharged time, ΔV is the potential window, and m denotes the mass of the electrode material. The quasi-triangular behavior of MWCNTs contributes to their reversible charge-discharge characteristics. Fig. 3 (d) illustrates the galvanostatic charge-discharge curves at current densities ranging from 0.5 to 5 A g^{-1}. A specific capacitance of 132 F g^{-1} was achieved at a discharge current density of 0.5 A g^{-1}. This higher capacitance value can be attributed to the accessible surface area created by the well-separated nanotube structure and functional groups, which enhance the wettability of the electrode for efficient electrolyte transport. Fig. 3 (e) shows the specific capacitances of 92.4, 77, 67, 64, and 55 F g^{-1} at 1, 2, 3, 4, and 5 A g^{-1} current densities, respectively. Fig. 3 (f) shows, the Nyquist plot for the MWCNTs electrode. The Nyquist plot of MWCNTs electrode exhibits a semicircle at higher frequencies and a straight line in the lower frequency region, confirming its capacitive behavior. The internal resistance (Rs) of approximately 1.9 Ω, a semicircle indicating charge transfer resistance (Rct) around 6.9 Ω, and a Warburg resistance attributed to diffusion processes are observed. At low frequencies, the Nyquist plot shows a nearly vertical line parallel to the imaginary axis, indicative of good capacitor behavior.

To evaluate practical performance, we investigated the capacitive properties of a solid-state ZIHC device utilizing MWCNTs nanostructure as cathode material and PVA-$ZnSO_4$ combinedly serving as the separator and solid electrolyte. Fig. 4 (a) displays an image of the designed ZIHC, while Fig. 4 (b) illustrates the CV curves at various scan rates.

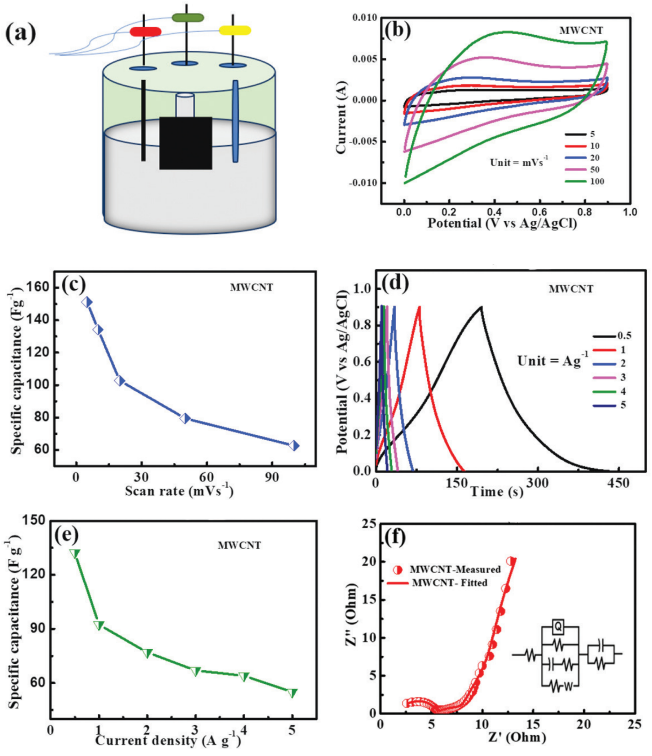
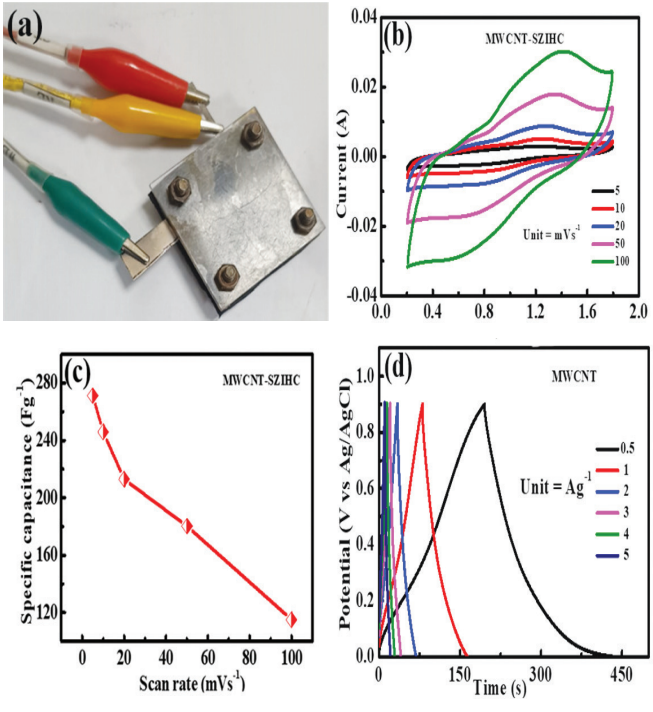


Fig.3(a) *Schematic diagram of 3 cell measurement,* ***(b)*** *CV curves* ***(c)*** *specific capacitance vs scan rate,* ***(d)*** *GCD curves,* ***(e)*** *specific capacitance vs current density, and* ***(f)*** *EIS plot for MWCNTs.*

The CV curves for the MWCNTs-based solid-state ZIHC indicate the formation of an electric double-

layer at the electrode-electrolyte interface, consistent across hybrid cell measurements. A small redox peak indicates the pseudo behavior due to the ion adsorption/desorption across electrodes but EDLC behavior still dominates. For the cell configuration, a maximum specific capacitance of 271.4 F g^{-1} was achieved at a scan rate of 5 mV s^{-1}. Also, Fig.5 (c) shows the specific capacitance of 246, 213, 180.3, and 115 Fg^{-1} at different voltage scan rates of 10, 20, 50, and 100 mVs^{-1}, respectively, further confirming that the MWCNT is the high sustainable materials for the ZIHC device. The galvanostatic charge-discharge (GCD) curves are the quantitative measurement of the energy storage of the ZIHCs, exhibiting quasi-triangular behavior (Fig. 4 d) with a specific capacitance of 221 F g^{-1} at a discharge current density of 1 A g^{-1} for the ZIHC device. Fig 4 (e) shows the specific capacitances 191.7, 145, 128, and 93.7 F g^{-1} at 2, 3, 4 and 5 A g^{-1} current density respectively, showing the high-rate capability of ZIHC. Figure 4(f) illustrates the electrochemical impedance spectrum for the MWCNTs-based solid-state ZIHC device. For the ZIHC device, Rs ~3.25 Ω and Rct ~12.7 Ω are observed, facilitating efficient charge transfer across the electrode-electrolyte interface due to good conductivity and high ECSA of MWCNTs.



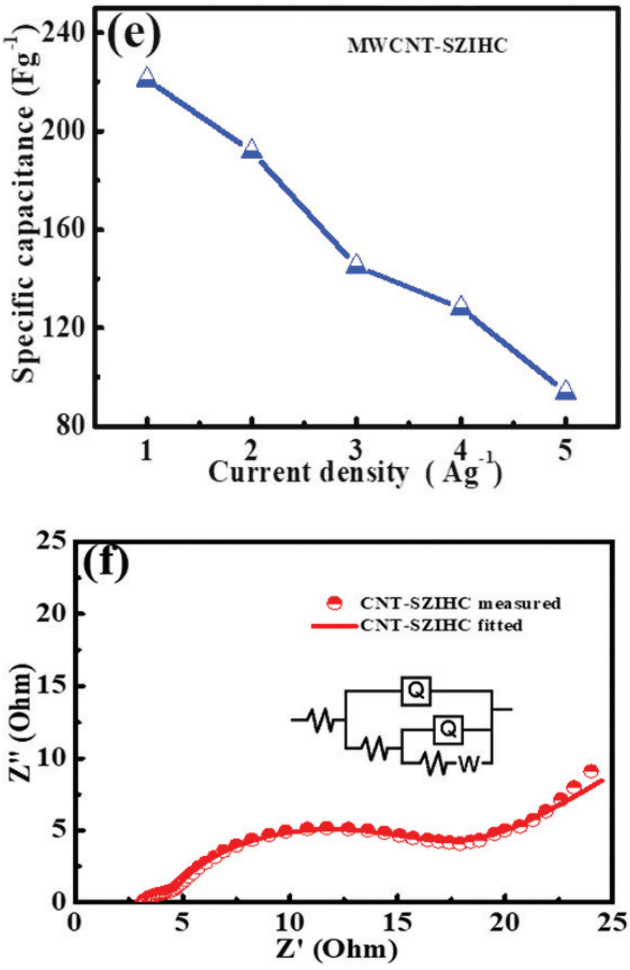


Fig.4 ***(a)*** *Photograph of ZIHC device,* ***(b)*** *CV curves,* ***(c)*** *specific capacitance vs scan rates* ***(d)*** *GCD curves,* ***(e)*** *specific capacitance at different current densities, and* ***(f)*** *EIS plot of MWCNT-based solid-state ZIHC device.*

We know that energy density determines how much energy ZIHC can store, while power density dictates how quickly they can charge and discharge, and cycle stability ensures their reliability over repeated use. These factors collectively define the effectiveness and practical utility of MWCNTs-based solid-state ZIHC in various high-performance applications. Fig. 5(a) depicts the Ragone plot of our device, highlighting its high energy density of 78.9 W h kg^{-1} at a power density of 800 W kg^{-1}. This performance is attributed to the efficient ion transfer between the electrolyte and electrode interfaces. The designed ZIHC device demonstrates high sustainable performance, achieving an excellent power density of 6400 W kg^{-1} alongside an energy

density of 19 W h kg^{-1}. Solid electrolytes enable higher energy density designs due to their ability to pack more active materials in a given volume or weight compared to liquid electrolytes. To assess stability, cyclic testing was conducted under a charge-discharge at a current density of 5 Ag^{-1}, revealing an impressive 89% capacitance retention over 8000 cycles (fig.4 b). The coloumbic efficiency of 100 % was also observed for our device. This performance is attributed to the stable nature of PVA-$ZnSO_4$ as electrolyte membrane and MWCNTs as cathode.

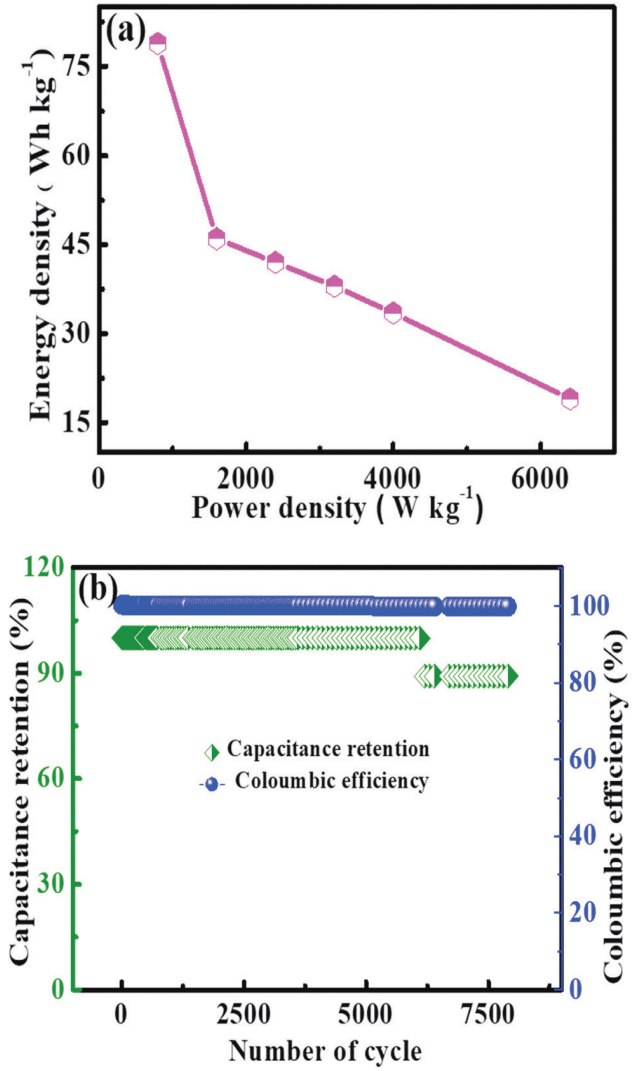


Fig.5 (a) *Ragone plot*, and ***(b)*** *stability performance of MWCNT-ZIHC.*

Conclusions

Here, we successfully synthesized MWCNTs via CVD method, where green tea extracts derived iron nanoparticles served as catalysts. The MWCNTs electrodes showed improved electrochemical performance in ZIHC, achieving a high specific capacitance of 221 F g^{-1} at 1 A g^{-1}, with an excellent energy density of 78.9 W h kg^{-1} at 800 W kg^{-1} power density, making it a promising energy device. Furthermore, the device exhibited 89% capacitance retention and 100% coulombic efficiency, demonstrating stability with the synthesized MWCNTs. This research offers important insights into optimizing the MWCNTs for applications in solid electrolyte zinc-ion hybrid capacitors.

Declaration of competing interest

The authors declare that they have no known competing financial interests or personal relationships that could have appeared to influence the work reported in this paper.

Acknowledgments

The authors acknowledge the support of IIT (BHU) for and its Central Instrument Facility for SEM and TEM study. AKM acknowledges the support of DST, India (grant no. IFA14-MS25). AP acknowledges UGC, India for providing the research fellowship.

Reference

1. J. Yin, W. Zhang, N. A. Alhebshi, N. Salah, and H. N. Alshareef, Adv Energy Mater **11**, 2100201 (2021).
2. A. K. Mishra and S. Ramaprabhu, J Nanosci Nanotechnol **12**, 6658 (2012).
3. S. Mishra, R. K. Gupta, and A. K. Mishra, Materials Science and Engineering: B **300**, 117129 (2024).
4. C. Singh, S. Nikhil, A. Jana, A. K. Mishra, and A. Paul, Chemical Communications **52**, 12661 (2016).
5. H. Liu, X. Liu, S. Wang, H. K. Liu, and L. Li, Energy Storage Mater **28**, 122 (2020).
6. H. Wang, Z. Wang, P. Bai, S. Hu, Y. Zhang, and R. Wang, Advances in Engineering Software **117**, 1 (2018).

7. S. Mishra, B. P. Majee, P. K. Maurya, and A. K. Mishra, Mater Res Express **6**, 088257 (2019).
8. Z. Li, Y. An, S. Dong, C. Chen, L. Wu, Y. Sun, and X. Zhang, Energy Storage Mater **31**, 252 (2020).
9. J. Liu, Z. Khanam, S. Ahmed, T. Wang, H. Wang, and S. Song, ACS Appl Mater Interfaces **13**, 16454 (2021).
10. A. K. Mishra and S. Ramaprabhu, AIP Adv **2**, 022121 (2012).
11. C. Singh, A. K. Mishra, and A. Paul, J Mater Chem A Mater **3**, 18557 (2015).
12. D. Zhang, L. Li, Y. Gao, Y. Wu, and J. Deng, ChemElectroChem **8**, 1541 (2021).
13. T. Lin, I. W. Chen, F. Liu, C. Yang, H. Bi, F. Xu, and F. Huang, Science (1979) **350**, 1508 (2015).
14. O. Okhay, A. Tkach, M. J. H. Gallo, G. Otero-Irurueta, S. Mikhalev, P. Staiti, and F. Lufrano, J Energy Storage **32**, 101839 (2020).
15. H. Chen, Y. Zheng, X. Zhu, W. Hong, Y. Tong, Y. Lu, G. Pei, Y. Pang, Z. Shen, and C. Guan, Mater Res Bull **139**, 111281 (2021).
16. S. Sarkar, A. Arya, U. K. Gaur, and A. Gaur, Biomass Bioenergy **142**, 105730 (2020).
17. A. Samage, M. Halakarni, H. Yoon, and N. Sanna Kotrappanavar, Carbon **219**, 118789 (2024).
18. K. Tang, L. Fu, R. J. White, L. Yu, M. M. Titirici, M. Antonietti, and J. Maier, Adv Energy Mater **2**, 873 (2012).
19. P. Liu, W. Liu, Y. Huang, P. Li, J. Yan, and K. Liu, Energy Storage Mater **25**, 858 (2020).
20. J. Huang, L. Wang, Z. Peng, M. Peng, L. Li, X. Tang, Y. Xu, L. Tan, K. Yuan, and Y. Chen, J Mater Chem A Mater **9**, 8435 (2021).
21. X. Chu, X. Zhao, Y. Zhou, Y. Wang, X. Han, Y. Zhou, J. Ma, Z. Wang, H. Huang, Z. Xu, C. Yan, H. Zhang, W. Yang, and J. Chen, Nano Energy **76**, 105179 (2020).
22. V. Sahu, R. B. Marichi, G. Singh, and R. K. Sharma, Electrochim Acta **240**, 146 (2017).
23. X. Chu, G. Chen, X. Xiao, Z. Wang, T. Yang, Z. Xu, H. Huang, Y. Wang, C. Yan, N. Chen, H. Zhang, W. Yang, J. Chen, X. Chu, Z. Wang, T. Yang, Z. Xu, H. Huang, Y. Wang, C. Yan, N. Chen, H. Zhang, W. Yang, G. Chen, X. Xiao, and J. Chen, Small **17**, 2100956 (2021).
24. X. Judez, H. Zhang, C. Li, G. G. Eshetu, J. A. González-Marcos, M. Armand, and L. M. Rodriguez-Martinez, J Electrochem Soc **165**, 6008 (2018).
25. W. G. Suci, H. K. Aliwarga, Y. R. Azinuddin, R. B. Setyawati, K. N. R. Stulasti, and A. Purwanto, Open Engineering **12**, 409 (2022).
26. V. Sahu, M. Mishra, G. Gupta, G. Singh, and R. K. Sharma, ACS Sustain Chem Eng **5**, 450 (2017).
27. S. Jung, Y. Myung, G. S. Das, A. Bhatnagar, J. W. Park, K. M. Tripathi, and T. Kim, New J Chem**. 44**, 7369 (2020).
28. B. Zhang, D. Wang, B. Yu, F. Zhou, and W. Liu, RSC Adv **4**, 2586 (2013).
29. D. Mohapatra, S. Badrayyana, and S. Parida, Mater Chem Phys **174**, 112 (2016).
30. B. Wei, M. Wen, Y. Zhao, C. Yang, J. Qiu, and L. Zang, Ionics (Kiel) **29**, 429 (2023).
31. H. Wang, M. Wang, and Y. Tang, Energy Storage Mater **13**, 1 (2018).
32. S. Chen, L. Ma, K. Zhang, M. Kamruzzaman, C. Zhi, and J. A. Zapien, J Mater Chem A Mater **7**, 7784 (2019).
33. N. Tripathi, V. Pavelyev, and S. S. Islam, Appl. Nanosci. **7**, 557 (2017).
34. B. M. Chufa, H. C. A. Murthy, B. A. Gonfa, and T. Y. Anshebo, Green Chem Lett Rev **14**, 640 (2021).
35. S. Mishra, S. S. Jaiswal, and A. K. Mishra, J. Mater. Sci.: Mater. Electron. **33**, 8702 (2022).
36. A. Aqel, K. M. M. A. El-Nour, R. A. A. Ammar, and A. Al-Warthan, Arab. J. Chem. **5**, 1 (2012).

37. M. Flygare and K. Svensson, Mater Today Commun **18**, 39 (2019).

38. E. Picheau, A. Impellizzeri, D. Rybkovskiy, M. Bayle, J. Y. Mevellec, F. Hof, H. Saadaoui, L. Noé, A. C. Torres Dias, J. L. Duvail, M. Monthioux, B. Humbert, P. Puech, C. P. Ewels, and A. Pénicaud, ACS Nano **15**, 596 (2021).

39. A. C. Ferrari and D. M. Basko, Nat. Nanotechnol **8**, 235 (2013).

40. P. K. Maurya and A. K. Mishra, J. Phys. Chem. Lett **15**, 1246 (2024).

41. P. Connor, J. Schuch, B. Kaiser, and W. Jaegermann, Zeitschrift Fur Physikalische Chemie **234**, 979 (2020).

42. S. Mishra, P. K. Maurya, and A. K. Mishra, Mater Chem Phys **255**, 123551 (2020).